Wildland Fire Rate of Spread Estimation Using an Autonomous Unmanned Aerial System: A Case Study

Bryce Ford *, Joon Tai Kim †, Ziyu Dong[‡], Roger Williams[§] and Mrinal Kumar [¶] *Ohio State University, Columbus, OH 43210*

This paper presents a case study of wildland fire rate of spread estimation using an autonomous unmanned aerial system (UAS), deployed in a prescribed burn conducted in the Zaleski State Forest in South Ohio. In recent years, UAS have seen increasing use to measure the fire perimeter in active wildland burns. In this case study, we build and deploy a small UAS platform equipped with infrared sensing to measure the rate of spread of the fire front in a prescribed burn conducted in a forest environment with significant topographic expression. Infrared data retrieved from the experiment is re-projected into the three-dimensional world frame, followed by a novel geometrical analysis of the observed fire intensity contours. A Delaunay triangulation is conducted to discretize the space around time-separated fire fronts, resulting in local rate of spread estimates based on fire intensity gradients. The infrared data-based rate of spread estimates are compared against the output of a widely used fire behavior model called the Rothermel model. While the data-based calculations show a good match with the Rothermel model's mean predictions, the latter is shown to exhibit large sensitivity to topographic and environmental parameters, especially slope steepness of the terrain.

I. Nomenclature

DEM = Digital Elevation Model EFB = Extreme Fire Behavior

FASMEE = Fire and Smoke Evaluation Experiment

FMI = Fuel Moisture Index

GIS = Geographic Information Systems

GOES = Geostationary Operational Environmental Satellites

h = Heat Content IR = Infrared

 $I_g(x, y)$ = Infrared Intensity in Cartesian Coordinates

 I_R = Reaction Intensity

MODIS = Moderate Resolution Imaging Spectroradiometer

MSG = Meteosat Second Generation NFDRS = National Fire Danger Rating System NWFG = National Wildfire Coordinating Group

ODNR-DF = Ohio Department of Natural Resources, Division of Forestry

 ξ = Propagating Flux Ratio

 ϕ_w = Wind Factor ϕ_s = Slope Factor ρ_b = Bulk Density

 ε = Effective Heating Number

 ρ_p = Particle Density

 M_x = Dead Fuel Moisture of Extinction

 δ = Fuel Bed Depth

^{*}Ph.D. Student, Mechanical and Aerospace Engineering, AIAA Student Member.

[†]Ph.D. Student, Mechanical and Aerospace Engineering, AIAA Student Member.

[‡]Ph.D. Student, School of Environment and Natural Resources.

[§] Associate Professor, School of Environment and Natural Resources.

[¶]Professor, Elizabeth Martin Tinkham Endowed Professor of Aeronautical and Astronautical Engineering, AIAA Associate Fellow.

 σ = Surface-Area-to-Volume Ratio

 M_f = Moisture content

PX4 = PixHawk 4 Autopilot System

QGC = Q-Ground Control Q_{ig} = Heat of Pre-ignition

R = Rothermel's Surface Fire Rate of Spread

ROS = Rate of Spread

 S_e = Effective Mineral Content S_T = Total Mineral Content $tan(\phi)$ = Slope steepness

 T_{rate} = Minimum Intensity Rate Threshold

 T_{ang} = Minimum Triangle Vector Gradient Threshold

 TV_i = i^{th} Triangle Vector U = Wind velocity

UAS = Unmanned Aerial System

 w_0 = Fuel Load

II. Introduction

A. Wildland Fire

Wildland fire is a widespread and fundamental ecosystem process that can contribute to the carbon cycle, subsequently influence the climate system via CO2 emissions [1], and can sustain specific fire-dependent ecosystems [2]. In recent decades, however, rapidly increasing fire activities have been observed due to a variety of factors, including fuel build-up, human activity, and climate change [3]. The subsequent fire regime shift has caused an increase in fire occurrence and size, and fire seasons now show a continued increasing trend in length with observed warming and drying, including within non-forest vegetation types [4]. These fire regime changes will heighten fire severity and drive the changes in vegetation composition [5]. For example, the predicted change in fire frequency and extent in the western U.S. is expected to transform the flora, fauna, and ecosystem processes in the Greater Yellowstone ecosystem, and there are indications that similar changes will occur for other subalpine or boreal forests [6].

Continuing changes in climate and fire regimes will increase the threat of larger and more frequent fires to fire-prone regions of the world [7]. Nonetheless, quantification of future trends in fire activity is challenging owing to the lack of spatially complete and consistently derived data [7]. Regional and spatial variability, complex and nonlinear interactions among weather, vegetation, and human activity added more uncertainty to future fire activities [8]. Therefore, understanding how fire behavior varies with local conditions, particularly the spatial and temporal distributions of flammable fuels, weather, and topography variation, is critical to predicting future fire behavior and quantifying fire propagation and intensity [9]. Indicators of fire spread characteristics include fire rate of spread (ROS), fire front location, residence time, and fire front intensity [10, 11]. These indicators are critical to describing forest fire behavior and predicting potential fire behavior changes [12] and can subsequently affect fire control plans and operations. However, accurate measurement and modeling of fire spread and associated parameters (e.g., fire ROS, flame front location, and flame intensity) are challenging owing to the fire's dynamic and complex characteristics [10]. The spatial and temporal differences combined with heterogeneous environmental conditions (weather, terrain, and vegetation) make it further complicated and uncertain to quantify fire propagation accurately [13, 14].

B. Prescribed Burns

As described in the previous section, fire has long been a disturbance that has shaped many of the North American ecosystems, whether these fires were ignited by lightning or Native Americans. Subsequently, many of these terrestrial ecosystems have evolved with dependence upon fire to maintain their presence on the landscape and their structure and function [15–17]. The European migration and settlement into North America during the 18th and 19th centuries brought significant changes to these fire regimes as wildfires became more rampant across the landscape followed by significant reductions in wildfire due to fire suppression policies and reductions in the use of fire by Native Americans [18]. This protracted period of fire exclusion has resulted in changes in the ecosystem composition, structure, and functions [19–21].

Prescribed fire, a planned fire used to meet management objectives, is becoming more commonly used and recommended as a means of reintroducing fire regimes to achieve ecological and restoration goals where fire has been excluded in the past and has caused changes to or even disappearance of ecosystems [22]. However, the reintroduction of fire is a more complex consideration, given that many ecosystems have been altered as the result of fire exclusion, and the corresponding response to fire may be different [23] and can produce undesirable effects [24]. The successful execution of a prescribed fire is defined by whether the specific management objectives have been met and, more importantly, whether the prescribed fire has escaped or not. The fear of escape by both managers and the public has become a disincentive for using prescribed fire as a management tool [18]. Therefore, weather (relative humidity, wind speed, direction, and air temperature) and fuel moisture conditions often need to occur in very narrow ranges such that the resulting fire behavior enables the fire to be managed and controlled.

C. Fire Behavior Analysis

Fire is an elastic phenomenon in that its behavior is influenced by factors of weather, fuel conditions, and topography where each of these individual factors themselves can exhibit great variability across the landscape. It is important to understand and predict fire behavior - for prescribed fires to remain under control and not escape, and for wildland fires to quickly be contained and extinguished. Accordingly, many models have been developed to predict fire behavior, and in particular, the rate of spread [25]. Fireline intensity, which is defined as the energy or heat release rate per unit time per unit length of the fire front, has been closely associated with ROS [26]. Fire intensity is also related to other aspects of fire behavior, such as flame height, flame depth, and the residence time of the flames at a point in the landscape [27]. Of great importance is the ability to predict extreme fire behavior (EFB), which has been defined by the National Wildfire Coordinating Group (NWFG) as a level of fire behavior characteristics that ordinarily precludes methods of direct control action [28]. In spite of the fact that many fire behavior models have been developed in attempts to predict fire behavior [25], accurate predictions are difficult to achieve because fires themselves can exercise different degrees of influence upon the environment in which they exist, thereby influencing their own behavior [28]. Ignition patterns for prescribed fires and suppression methods used in combating wildfires are often determined by expected and current fire behavior [29]. Many of the current fire behavior models often generalize expected behavior based on a given fuel model type with the ability to input influential parameters such as fuel moisture, wind speed, relative humidity, and slope. However, these models do not account for the variations that can occur within a fuel model type, nor do they account for the fire's self influence on fire behavior. While topographic features do not change, the weather parameters change with time, requiring new inputs into the prediction model to get updated fire behavior predictions. However, these models cannot capture the fire's influence on the fire environment and resulting behavior.

The ability to develop and use active sensing methods that can measure a fire's current behavior in the context of its environment and the behavioral changes has become paramount as large wildfires are becoming more frequent across the globe [30, 31]. Sensor data can be employed to determine ROS, fire intensity, flame length, and the more minute changes in the fuel model type across the landscape. Aerial sensors can provide critical real-time changes in fire behavior, providing more accurate predictions of short-term fire behavior. In recent years, the use of robotic agents to assist during the various phases of planning and execution of a prescribed burn, as well as in wildfire management, has gained momentum. Ref.[32] presents a review of recent efforts to leverage satellite data for the advancement of wildland fire science (in particular, the development of fire behavior predictive models) and fire management. Orbital platforms such as Geostationary Operational Environmental Satellites (GOES), Moderate Resolution Imaging Spectroradiometer (MODIS), Sentinel-1, and Meteosat Second Generation (MSG), to name just a few, have served research efforts for pre-fire analysis, early and active fire detection [33], as well as active fire monitoring and prediction [34]. Ref.[35] outlines early work in the use of sub-orbital (aerial) remote sensing to increase the spatial resolution of fuel data to improve wildfire spread predictions. A wide range of sensing modalities such as LiDAR, multispectral and hyperspectral imaging can be effectively deployed on aerial platforms. For instance, Ref. [36] is an early work that combined infrared and color photogrammetry with extensive fieldwork to compile crucial fuel properties such as canopy cover, tree height, and crown bulk density for use in three-dimensional fire simulation models. In recent years, there has been increasing activity in unmanned aerial systems (UAS)-based imaging systems to profile under-canopy fuels and forest structure, e.g., to reveal the presence of ladder fuels [37, 38]. UAS are now also being employed during active fires with increasing regularity to retrieve data from the fire perimeter, especially during prescribed burns. In a recent study, Ref.[39] used airborne thermal infrared imagery to estimate fire ROS, demonstrating the importance of infrared imagery for understanding fire behavior and suggesting the high variation of fire spread at a local scale. In Ref. [12] employed UAS-mounted thermal imagery to compute the rate of spread in a prescribed grass fire. Over the next five years (2023-2027), NASA will integrate a wide range of orbital and sub-orbital sensing platforms, including UAS, within a multi-agency, interdisciplinary collaborative effort titled "Fire and Smoke Evaluation Experiment" (FASMEE) [40]. In this series of large prescribed burn campaigns, UAS-based multi-modal sensors will collect data during pre-fire (fuel characterization), active fire (ROS, intensity), and post-fire (burn area, severity, air quality).

D. Objectives and Contributions

As mentioned above, rate of spread is a primary indicator of fire behavior. It is defined as the rate of forward advancement of the flame front in a spreading fire [41]. Accurate determination of ROS is critical from both practical and scientific perspectives, since it is directly related to fire intensity and fire front geometry [42], and it can be used to assess fire risk by estimating the fire front arrival times, potential fire growth path, and fire extent [10]. Past studies have developed various methods to quantify fire ROS, including mathematical models and related software [43-45]. For example, the Rothermel mathematical model was created based on the principles of conservation of energy to predict one-dimensional fire ROS [25]. This model was reformulated and further developed in Ref.[46], enabling it for use in heterogeneous fuel bed conditions. Ref.[44] implemented the Rothermel fire spread model in ArcGIS and simulated the propagation of a forest fire given a fire ignition point. In order to quantify the fire ROS accurately, a better methodology regarding fire spread direction and distance at different time series is needed. This work employs UAS-based infrared imagery for ROS computation in a prescribed burn conducted in a forest environment with significant topographic expression. The objectives of this study are to 1) quantify fire ROS using infrared (IR) images based on real-fire data at a local scale, 2) Estimate fire ROS using the Rothermel fire spread model, and 3) present a detailed comparison between the data-based ROS computation and Rothermal model output, resulting in a validation study of the latter. A small-sized quadrotor UAS (500 mm, 3041 grams without payload) named Bluebird is constructed to carry infrared (IR) sensing equipment during a prescribed burn. Bluebird is deployed in a prescribed burn conducted by ODNR-DF in the Zaleski State Forest in South Ohio at a burn site with considerable topographic relief. Autonomous flights are conducted with the IR sensor on board that returns fire imagery. Raw camera data is re-projected into the 3D world frame. This is followed by a novel geometrical analysis that identifies the fire front and fire perimeter at time intervals 10 seconds apart. Delaunay triangulation based segmentation of the space between the evolved fire front is conducted to derive fire vectors based on the fire intensity index. The linear rate of spread and spreading area per unit of time is calculated as a method to evaluate fire behavior and fire risk. IR data-based ROS computations match well with mean Rothermel model outputs. However, significant variability in the Rothermel model output is demonstrated due to its sensitivity to topographic and environmental parameters, especially slope steepness.

III. Methodology

A. Study Site and Prescribed Fire Parameters

The study area is located at Zaleski State Forest (82°25'W, 39°18'N) in Vinton County, Ohio. This area lies on the unglaciated Appalachian Plateau, which consists of steep hills and valleys and is the most rugged area in the state. As shown in Fig.(1), an area of 58 hectares located within Zaleski State Forest, referred to as Morgan Hollow, was selected for this study. On 21 March 2022, from 11:30 am to 3:30 pm, a prescribed forest fire was conducted on Morgan Hollow with a mean wind speed of 2.68 mph and a direction from the south. The ambient temperature was around 13.6°C, while the relevant humidity was around 20.22% based on the weather data from a Davis Vantage Vue Weather Station. In collaboration with the Ohio Department of Natural Resources, Division of Forestry (ODNR-DF), the prescribed fire was conducted by using a ring pattern ignition and burned mainly through broadleaf forest fuel (Quercus. alba L., Quercus. rubra L., Acer rubrum L., Fagus grandifolia Ehrhart, and Nyssa sylvatica Marsh.). Two crew teams ignited the site with drip torches starting from the northeast corner of Morgan Hollow and moved in opposite directions along the boundaries of the Morgan Hollow and met around the southwest corner, which allowed the fire spread towards the center of the study site from the boundaries.

B. UAS Platform

Autonomous UAS play a key role in the safe and economical monitoring of prescribed burns and wildfires. The nature of the wildland burn environment in this study requires a UAS to operate beyond visual line of sight, so the platform must be able to reliably perform autonomous actions, such as waypoint tracking. Many commercially available off-the-shelf UAS exist, such as DJI Mavic 3[©], that are capable of flying in a prescribed burn environment. However,

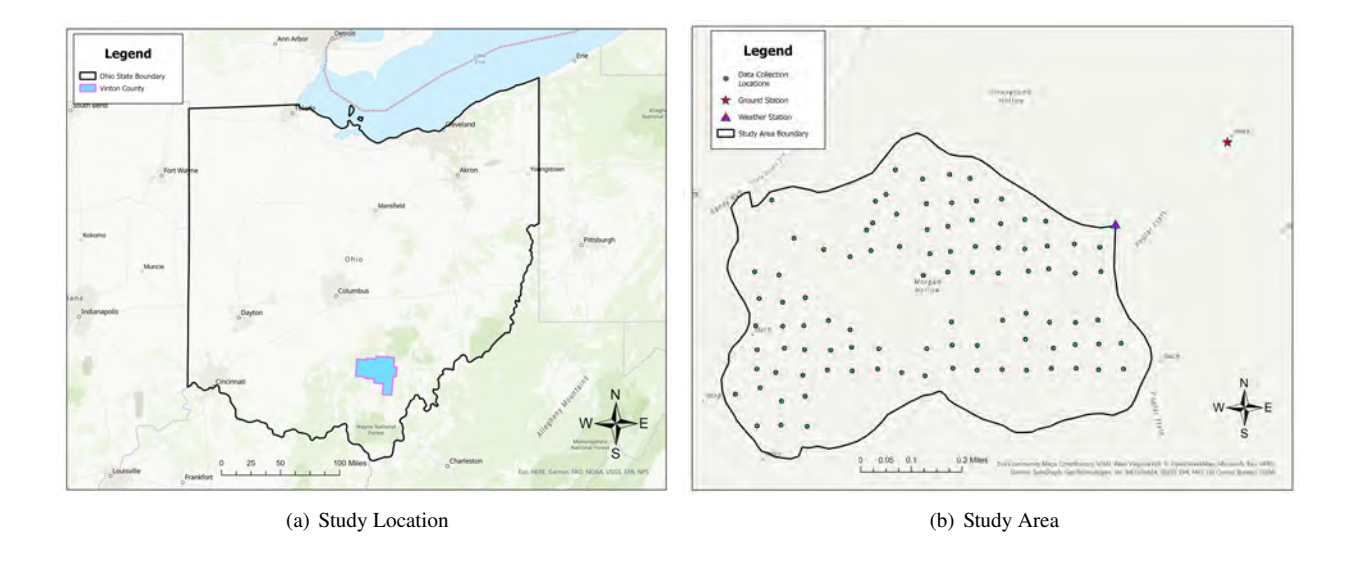


Fig. 1 Maps of Study Area and Landmarks

their source code is closed-source and inflexible in their operation. In order to achieve autonomous capabilities required

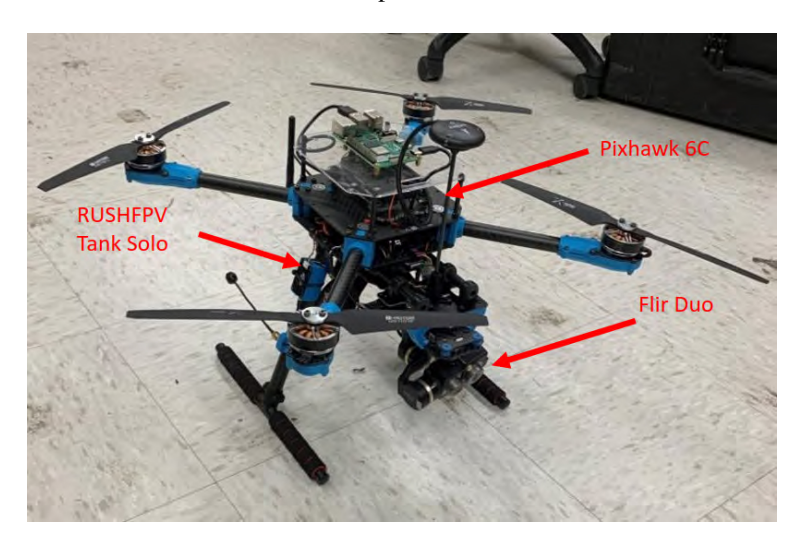


Fig. 2 BlueBird UAS Platform

for a UAS to fly in a wildfire environment, with required sensor integration to capture an evolving fire perimeter, an open-source flight controller was chosen. Pixhawk 4 (PX4) Autopilot is an open-source flight stack that is compatible with many off-the-shelf drone components. To complement the PX4 flight controller, the HolyBro X500 V2 was chosen as the frame. The X500 V2 provides quick access to the Pixhawk board, which makes servicing the platform simple. Aikon 32-bit 35A ESCs paired with TMotor MN3110 motors and TMotor MS1101 11"×4.2" propellers were used as the propulsion system. Additionally, the airframe is equipped with a GPS receiver, a Radio Control receiver (2.4 Ghz), a telemetry receiver (915 Mhz), and a RUSHFPV Tank Solo (5.8 Ghz) video transmitter to allow for the pilot to select points of interest remotely. This system was dubbed the *BlueBird* and can be seen in Fig.(2). The BlueBird can be commanded via telemetry using a laptop running QGroundControl [47]. QGroundControl is an open-source ground station application that can communicate with Pixhawk flight control boards using the MAVLink, an open-source micro air vehicle marshaling protocol [48]. Using QGroundControl, the pilot can command the UAS to change flight modes, take off, land in place, return to home, and plan and manage basic waypoint tracking missions. The BlueBird could also be controlled manually using a FrSky Taranis X9D remote controller. This allows for manual control of the UAS's

position, attitude, and camera gimbal position if needed. The BlueBird could be mounted with a companion computer, i.e. a computer that does not handle the PX4 flight stack and is able to perform guidance, navigation, and control tasks supporting the flight controller. The Bluebird platform shown in Fig.(2) measures 500 mm diagonally (motor-to-motor) and weighs in at 1675 grams without a battery. With a Turnigy 4S 16000 mAh LiPo installed on the frame, the platform weighs 3041 grams and delivers a flight time of 23 minutes.

C. Sensing

A FLIR Duo camera was used to capture the fire perimeter. The FLIR Duo is capable of recording Infrared and RGB video simultaneously. Infrared video is required to track the fire when it is obscured by smoke and trees. The FLIR Duo is not capable of radiometry and instead maps the intensity of each pixel relative to the range of infrared intensity in the image, as can be seen in Fig. 3. The infrared images are tagged with BlueBird's pose, allowing each image to be

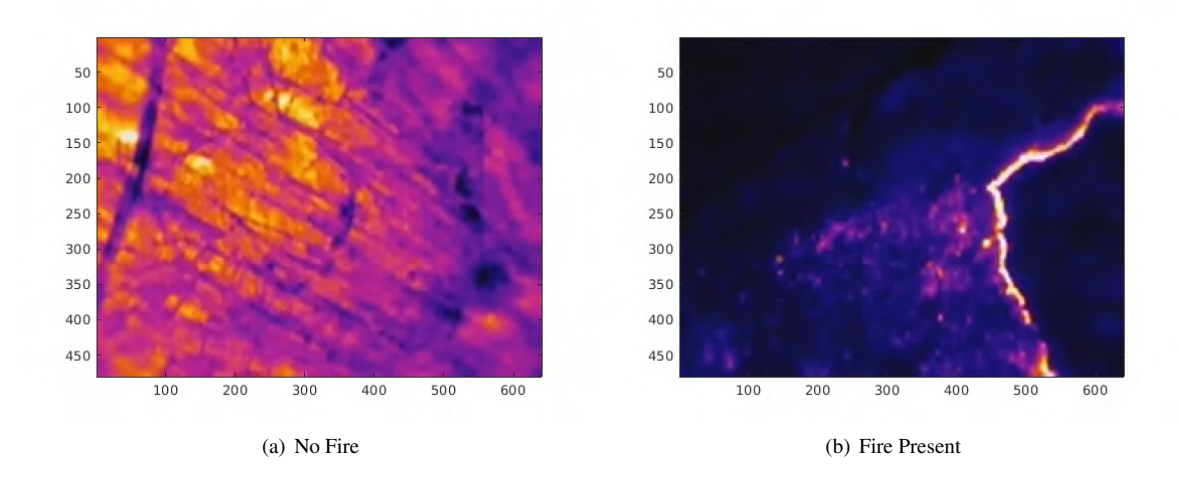


Fig. 3 Low and high infrared intensity images are compared. When a fire is present, the unburnt forest floor dominates the infrared intensity range, but when a fire is present in the image, the intensity is separated between the forest floor and the fire.

localized in the global frame. BlueBird's position is set to the position of the image. The BlueBird UAS system is unable to record the pose of the gimbal relative to the flight controller, so the FLIR Duo is assumed to be pointing straight down from BlueBird. The FLIR Duo was pointed nadir for all observing segments of BlueBird's missions, but there is no method to verify that it was perfectly pointed down in every instance. This is a source of error to be considered in the analysis.

D. Data Analysis

Image Reprojection

Infrared intensity images must be re-projected from the 2D image frame into the 3D world frame. This is performed using the UAS's estimated pose, the terrain altitude surface, and the camera-intrinsic properties of the FLIR Duo. This work employs the pinhole camera model for the purpose of re-projection. Each pixel coordinate is mapped from the image frame to a corresponding point in the camera frame using the intrinsic calibration matrix defined by the FLIR Duo. The camera frame is then mapped into the world frame using BlueBird's pose information as its extrinsic calibration. The image can now be projected onto the terrain surface. A Delaunay triangulation is used to construct a surface out of geo-referenced terrain altitude data to construct the terrain surface. Rays originating from the pixels defined in the global frame are projected onto the surface. The mapping of each pixel to the terrain surface is constructed by computing the intersection point of each ray with the triangles that define the surface. A resulting re-projected image can be seen in Fig.(4).

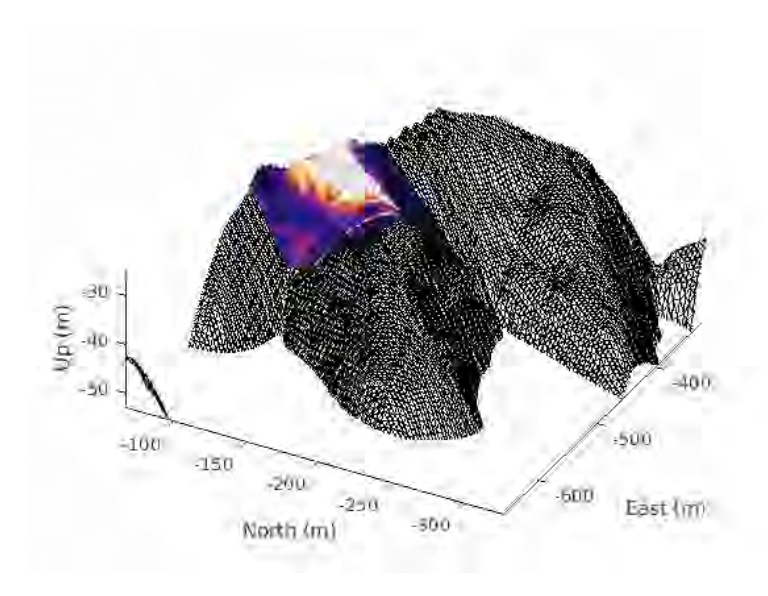


Fig. 4 Infrared Image Projected Onto Terrain Surface

Rate of Spread Computation

ROS captures how quickly the fire is spreading. It is commonly expressed in units of feet per second. Fire front position and front intensity are important metrics of fire behavior that are directly related to fire ROS. The fire front is the interface between burnt and unburnt areas in remote sensing or infrared images, which can be identified with specific criteria, such as intensity, color information, and fire shape [49]. The fire front, specifically the head of the fire, is the fire section with the fastest spreading velocities and highest intensities [50]. Recent works have focused on the accurate delineation of active fire front positions as it can be used as a function to calculate fire ROS [51]. Ref.[14] estimated fire ROS by delineating active fire front locations at different time intervals and generating fire spread vectors between those fire front curves. In Ref.[14], the direction of each fire spread vector that was used as a distance to calculate the fire ROS was automatically determined by ArcGIS software, which may not be accurate to represent the real fire spread direction, and subsequently will affect the accuracy of the distance of each vector and influence the results of fire ROS. Regarding the variable fire environment and fire characteristics (fire ROS, fire intensity, and fire front position) at the fine scale, emphasis should be placed on the accuracy of the mathematical model and IR image processing. Besides, a comparison of different methods to quantify fire spread based on the same landscape location and fine-scale field data are critical to providing a better understanding of fire spread accuracy.

ROS can be computed by tracking the movement of temperature contours between infrared images of the fire [14]. A temperature or intensity must be chosen to represent the boundary of the fire. This is impossible in the Zaleski Forest prescribed fire dataset as radiometric data is not available. Only the relative fire intensity within the image is available. An arbitrary threshold must be chosen to represent the fire boundary. When fire is present in infrared images taken by the FLIR Duo in contrast to the forest floor, the intensity is grouped between its maximum and minimum values. If the contour value is picked between these two extremes, the fire boundary can be constructed as shown in Fig.(5). Even if the exact location of the contour changes when different intensities are selected, this change will be consistent between images as long as the contrast between fire and the unburned forest floor is present in the image. Given two contours mapped into the world frame, the core problem is describing how the contours moved between time stamps. ROS is a velocity, not the rate of change in the area of the fire. This means that computing the additional area occupied by the fire is insufficient. Additionally, the ROS can not be negative. Simply observing the contours can result in apparent negative ROS values. This is because when the intensity contour is expanding, the fire consumes more unburned area, while when the intensity contour is contracting, the fire is merely cooling down. Considering this, a common method for computing the rate of spread from the contours is to use tangent vectors like in Ref.[12]. Tangent vectors from the original contour are projected towards the second contour, as can be seen in Fig.(6). The ROS is the vector length over the Δt between the contours. This procedure is a straightforward way to estimate the local ROS of a firefront but suffers from the major drawback that relevant areas of the fire contours must be selected by hand. It performs well if the fire is visibly spreading "outward" in all directions. However, it cannot be applied to more complex contours, as can be seen in

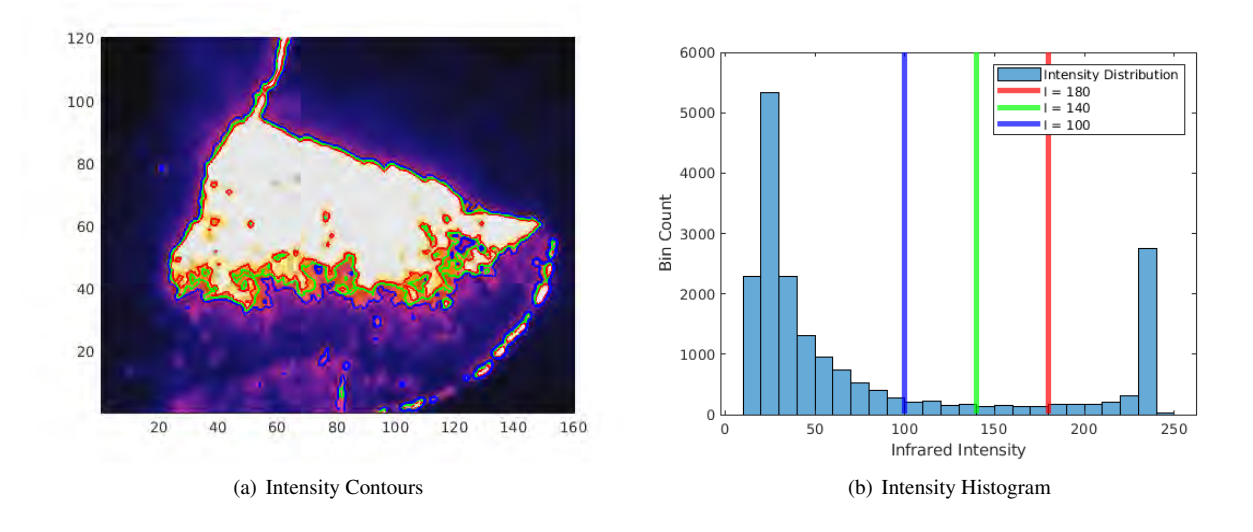


Fig. 5 Comparing Intensity Thresholds to Define The Fire Boundary

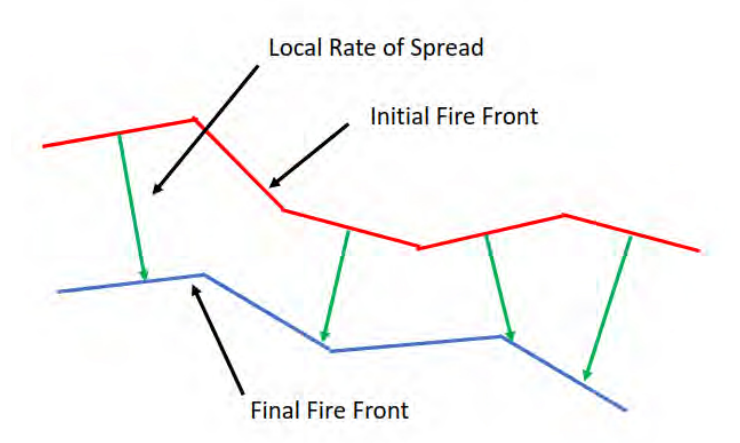


Fig. 6 Tangent Vector Rate Of Spread: The blue contour represents the initial fire front, and the red contour represents the final fire front. The length of the green tangent vectors represents the local ROS.

Fig.(7). It is unable to distinguish between expanding and contracting contours, so the contours it is applied to must be manually selected to prevent this.

A new method is introduced to compute ROS that is able to handle complex fire intensity contours. The first step is to simplify the complexity of the fire contours. The contours are often fragmented between multiple polygons and not necessarily closed, as can be seen in Fig.(7). A Delaunay triangulation is used to partition the space between and around the contours into simple triangles, as can be seen in Fig.(8). Using the triangulation, the area between the contours can be classified as "newly burned" or "cooling fire". Two measures are used to classify the triangulation. The first measure is the time derivative of the intensity. This can be expressed as:

$$\max\left(\frac{\partial}{\partial t}(I_g(x_{c,i}, y_{c,i})), \ 0\right) \ge T_{rate} \tag{1}$$

where I_g is the intensity mapped to the global frame, $(x_{c,i}, y_{c,i})$ is the center of the i^{th} triangle, and the T_{rate} is the minimum rate of intensity increase for the fire to be considered expanding. For the fire to have spread, the intensity must have increased over Δt , so the time derivative of the intensity must be positive. As can be seen in Fig.(9), the regions

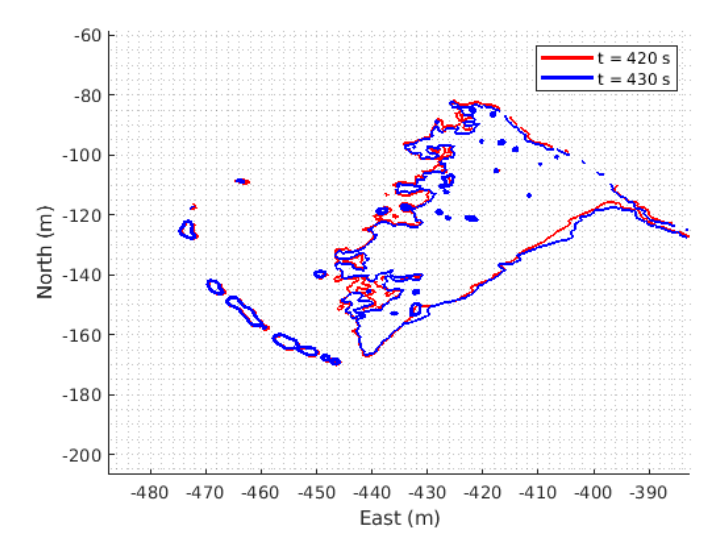


Fig. 7 I = 140 contours at t = 420s and t = 430s projected onto the terrain surface.

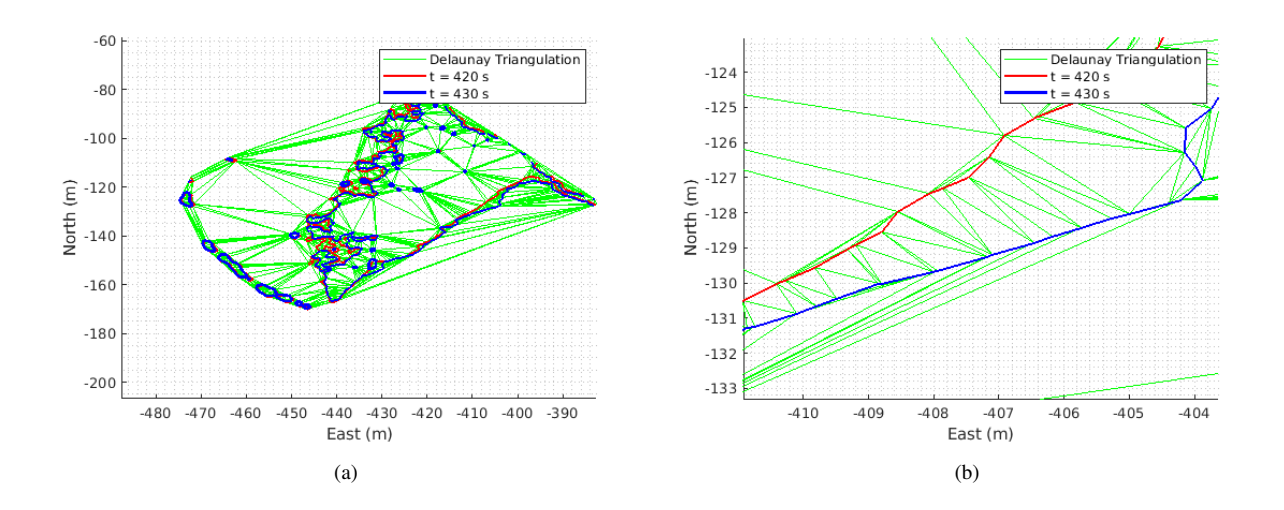


Fig. 8 Delaunay triangulation is used to partition the space between the two contours.

where the rate of intensity change is positive readily identify where the fire expanded. There is a lower bound on the rate of intensity increase for a triangle to be considered because there can be small fluctuations in the middle of the fire and unburned regions, which can lead to misclassifications.

The second measure is the direction of the gradient of the intensity. The gradient of the intensity will, by definition, point from the high fire intensity regions toward cooler regions. Triangles that are comprised of vertices on both the initial and final contour can be given direction. This is done by constructing a vector that connects the edge/vertex on the initial contour to the edge/vertex on the final contour, as can be seen in Fig.(10). If the triangle vector and the intensity gradient are pointing in the same direction, the contour moved towards the high intensity region of the fire. This implies that the fire cooled in that region. If the triangle vector points in the opposite direction as the intensity gradient, the contour moved away from the high intensity region of the fire. This implies that the fire expanded in that region. This condition can be constructed using the angle between the gradient and the triangle vector as follows:

$$\arccos\left(\frac{\nabla I(x_{c,i}, y_{c,i}) \cdot TV_i}{\|\nabla I(x_{c,i}, y_{c,i})\| \|TV_i\|}\right) \ge T_{ang}$$
(2)

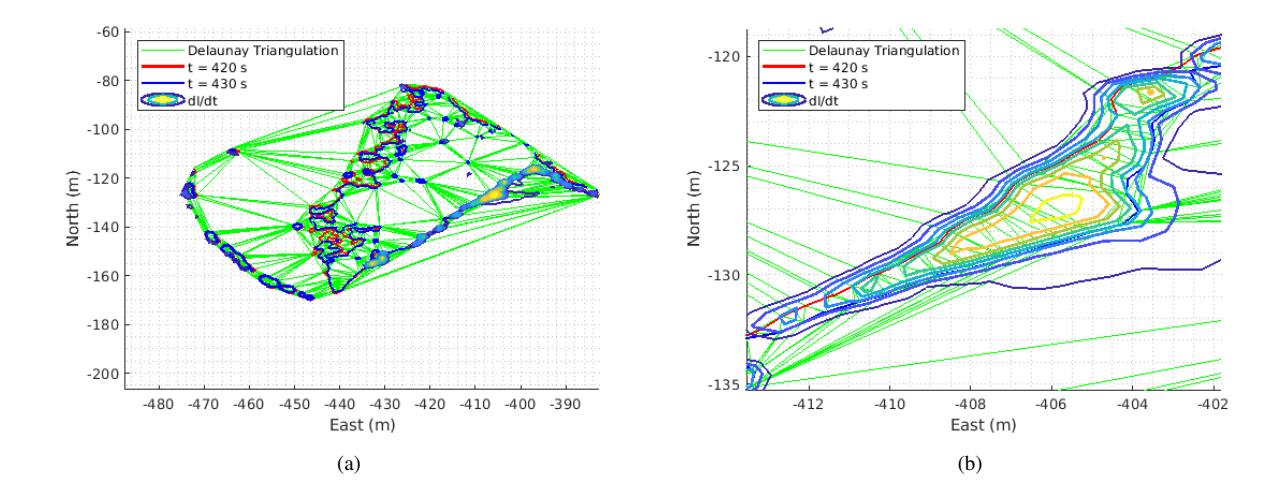


Fig. 9 $\max\left(\frac{\partial I_g}{\partial t},0\right)$ overlayed on the contour defined Delaunay triangulation.

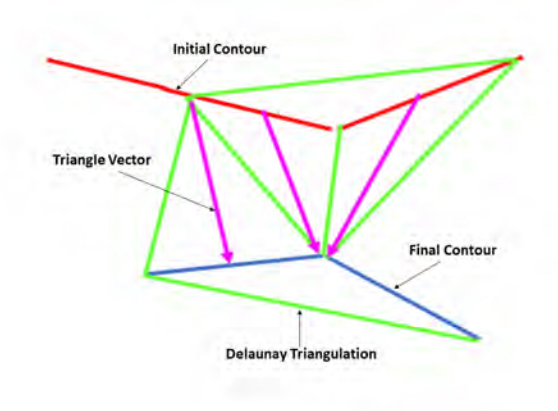


Fig. 10 The red line describes the initial contour, and the blue line describes the final contour. Green lines and contour lines make up the Delaunay triangulation. Magenta arrows represent the vector connecting the two contours when available in a given triangle.

where $\nabla I(x_{c,i},y_{c,i})$ is the gradient of the intensity at the center of the i^{th} triangle, and TV_i is the i^{th} triangle vector. This is seen in Fig.(11). The threshold T_{ang} sets a lower limit of the angle between the vectors to be considered pointing in opposite directions. Using both conditions, described in Eq.(1) and Eq.(2), in conjunction, the triangles can be reliably classified as spreading fire or not. The rate of spread at a given triangle that is classified as spreading fire is defined as $ROS = ||TV_i||/\Delta t$ and is located at the center of the triangle that defines it. Fig.(18) shows a set of fully classified contours.

E. The Rothermel Surface Fire Spread Model

The results of IR data analysis described in the above sections produced ROS estimates, which are presented in Sec.(IV.A). This section presents an overview of the Rothermel fire spread model. A detailed account of this model is available in Ref.[25]. The model described in Ref.[25] is based on the foundations provided by Rothermel's surface fire spread model [52], with some adjustments implemented in Ref.[53]. Excluding the environmental parameters that were collected throughout this study, the nominal values for fuel parameters suggested in Ref.[25] were utilized. Subsequently, based on statistical analysis and measurements of central tendency, several ROS estimates were computed and compared with the IR data-based ROS results.

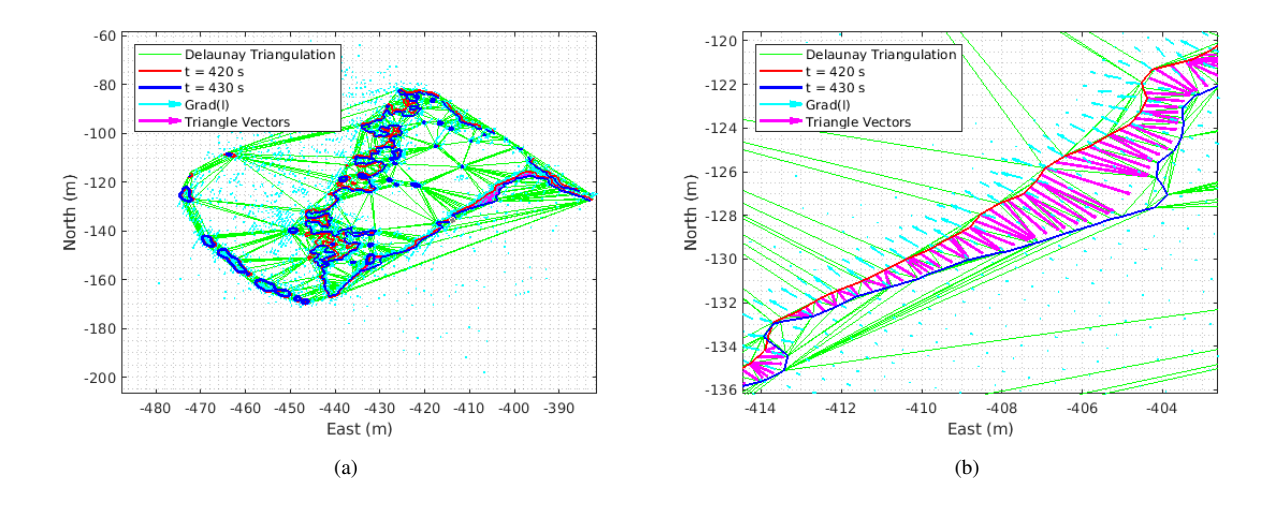


Fig. 11 $\nabla I(x_{c,i}, y_{c,i})$ overlayed on triangle vectors defined by the Delaunay triangulation.

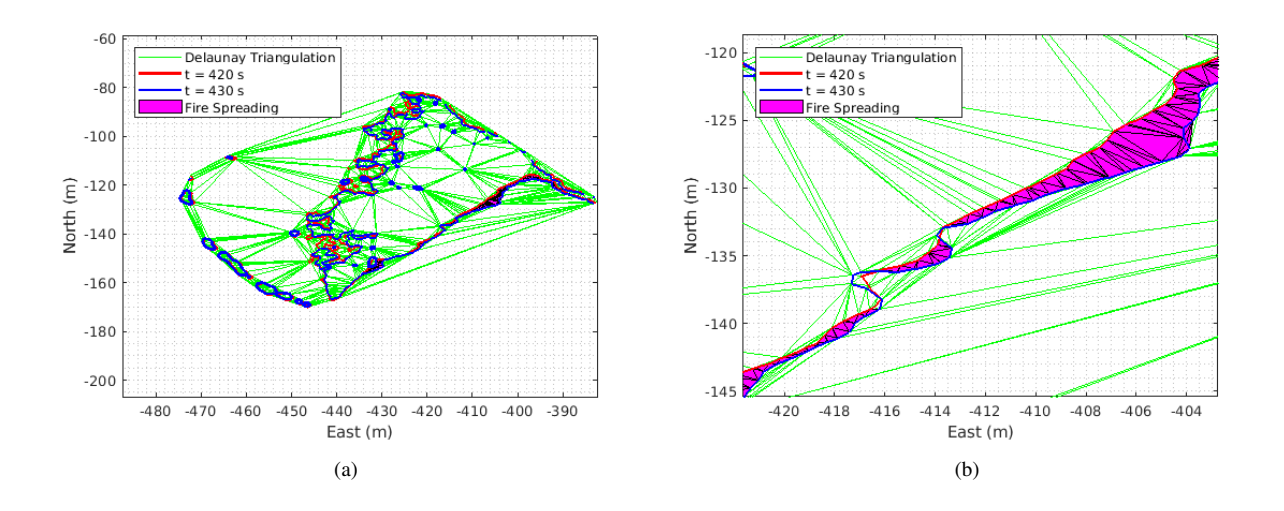


Fig. 12 Eq.(1) and Eq.(2) used to classify triangles defined by the Delaunay triangulation of the intensity contours.

1. Model Background

The Rothermel surface fire spread model, developed originally by Richard C. Rothermel, is one of the most widely utilized models in fire behavior research, fire management, and safety procedures since 1972[25]. Based on the heat balance model developed in Ref.[54], this quasi-empirical model is designed to estimate the ROS and intensity of quasi-steady state fires in wildland terrains, such as grasslands and forests. Fundamentally, this model integrates fuel properties, topography, and weather conditions to predict fire behavior. Today, the Rothermel model remains an important tool in fire behavior prediction and various fire management planning methods, such as the National Fire Danger Rating System (NFDRS) [55]. It helps fire managers and researchers assess potential fire behavior, plan firefighting tactics, and effectively allocate resources. The model is frequently used with environmental data and geographic information systems (GIS) to create fire characteristic maps and support the decision-making of fire management personnel during wildfire outbreaks [56].

2. Model Framework

At its core, the Rothermel model is based on the physical and chemical characteristics of fire spread while considering the conservation of energy between the fire and its surroundings [57]. It assumes that the fuel particle properties, the availability and arrangement of fuel, and various environmental factors determine ROS. The model calculates the ROS using empirical relationships and yields an estimate of other fire behavior characteristics, such as flame length and fireline intensity [25]. The basic ROS model that applies a single-sized class of dead fuel per calculation was employed in our study. Rothermel defines the final ROS equation [52] as:

$$R = \frac{I_R \xi (1 + \phi_w + \phi_s)}{\rho_b \varepsilon Q_{ig}} \tag{3}$$

Rothermel's ROS equation consists of two main parts: the *heat source* (numerator) and the *heat sink* (denominator). The reader is referred to *Table* (1) and *Table* (3) in Ref.[25] for empirically derived relationships to express the constitutive elements of these two main parts. These nominal values are employed as input parameters and then inserted as values into relevant equations for ROS calculation in accordance. A brief description of the heat source and heat sink elements is provided below for completeness.

A) Heat Source. The numerator of Rothermel's ROS model is defined as the heat source. It represents the rate of heat released from the fire into the fuel bed located in front of the head fire [25]. It consists of the reaction intensity component (I_R) , the propagating flux ratio (ξ) , the wind factor (ϕ_w) , and the slope factor (ϕ_w) . Table (1) outlines the various components of the heat source.

Component	Symbol	Definition
Reaction Intensity	I_R	The total amount of heat release rate per unit area of the fire front.
Propagating Flux Ratio	ξ	The portion of the Reaction Intensity that directly heats neighboring fuel to ignition.
Wind Factor	ϕ_w	Dimensionless multiplier that represent the effects of wind in Rothermel's ROS equation.
Slope Factor	ϕ_s	Dimensionless multiplier that represent the effects of slope in Rothermel's ROS equation.

Table 1 Heat Source Components

B) Heat Sink. The denominator of Rothermel's ROS model is defined as the heat sink. It is the amount of heat needed to ignite the fuel. This depends upon the fuel ignition temperature, fuel moisture content, and the amount of fuel included in the fuel ignition procedure [25]. The parameters contributing to the heat sink term include bulk density (ρ_b) , the effective heating number (ε) , and the heat of pre-ignition (Q_{ig}) . In sum, Table (2) describes the heat sink's components. The reader is referred to Ref.[25] for additional details.

Table 2	Heat Sink	Components

Component	Symbol	Definition	
Bulk Density	$ ho_b$	The total amount of oven-dry (anhydrous state) fuel per cubic foot of fuel bed.	
Effective Heating Number	ε	The portion of fuel particle that is heated to ignition temperature upon ignition of fuel.	
Heat of Pre-ignition	Q_{ig}	The heat needed to ignite a pound of fuel.	

C) Input Parameters. Table (3) shows that the basic Rothermel model has three input categories: fuel particle properties, fuel array arrangements, and environmental values. The fuel particles and fuel array parameters are intrinsic components

of the Rothermel ROS model that are typically maintained as constants. We utilize the suggested nominal values that are referenced in *Table (2)* and *Table (8e)* of Ref.[25]. All three environmental parameter values were based

 Table 3
 Input Parameters (Single-sized Class of Dead Fuel: Fuel Model TL6)

Category	Parameter (Unit)	Symbol	Remarks
Fuel Particles ¹			
	Heat Content (Btu/lb)	h	$8,\!000\;Btu/lb$
	Effective Mineral Content (fraction)	S_e	0.0010 (<i>lb</i> minerals - <i>lb</i> silica) / <i>lb</i> wood
	Total Mineral Content (fraction)	S_T	0.0555 lb minerals / lb wood
	Particle Density (lb/ft ³)	ρ_p	$32 lb/ft^3$
Fuel Array ²			
	Dead Fuel Moisture of Extinction (fraction)	M_{x}	0.25 %
	Fuel Bed Depth (ft)	δ	0.3 ft (mean value)
	Fuel Load (lb/ft^3) w_0		$0.1102 \ lb/ft^3$
	Surface-Area-to-Volume Ratio (ft^{-1})	σ	$2,000 \ ft^{-1}$
Environmental Components			
	Moisture content (fraction)	M_f	Eq.(4)
	Slope steepness (fraction)	$\tan \phi$	Vertical rise / horizontal distance
	Wind velocity (ft/min)	U	Measured at midflame height

¹These nominal values were used for this category in our study, as suggested by Albini [25, 53].

on measurements from data that were collected on-site before and during the prescribed burn. The methods for environmental data collection are explained in Sec. (IV.B.1). According to the Rothermel model, the wind speed is at midflame height. This model was designed to predict ROS while exploiting fuel and environmental conditions where a fire is assumed to spread [25]. Therefore, in most applications, the human eye level of approximately 5.5 ft is generally considered a reference for midflame heights [58]. Finally, a choice of different models could be adopted to express the fuel moisture content in Rothermel's ROS model, such as the regression-based model of Ref.[59] or a semi-physical model as described in Ref.[60]. In this work, the fuel moisture index (FMI) model formulated in Ref.[61] was used due to its computational robustness and simplicity. FMI is defined as a function of dry-bulb temperature (°C) and relative humidity (fraction) and expressed in Eq.(4) [62] below.

$$FMI = 10 - 0.25(T - H) \tag{4}$$

IV. Results

A. IR Image-based Rate of Spread Output

Fig.(13) represents the two IR video/image data collection areas. As described in Sec.(III.C) and Sec.(III.D), the rates of spread at given points are geo-referenced to GPS coordinates in the study area, Fig.(1(b)), and mapped using the ArcGIS Pro software. Region I has an area of 49.86×10^4 ft^2 and is located in the northeastern region of the study plot. On the other hand, Region II has an area of 1.85×10^5 ft^2 and is located in the north/central region.

IR-data Collection in Region I

As illustrated in Table 4, a total of 1384 points were evaluated during five 10-second intervals for Region I. Using the methods described in Sec.(III.D), statistical analysis shows that the ROS range in Region I lies between 0.93 ft/min

² Nominal values for fuel model TL6 (Moderate load broad-leaf litter) were used for this category in this study [25].

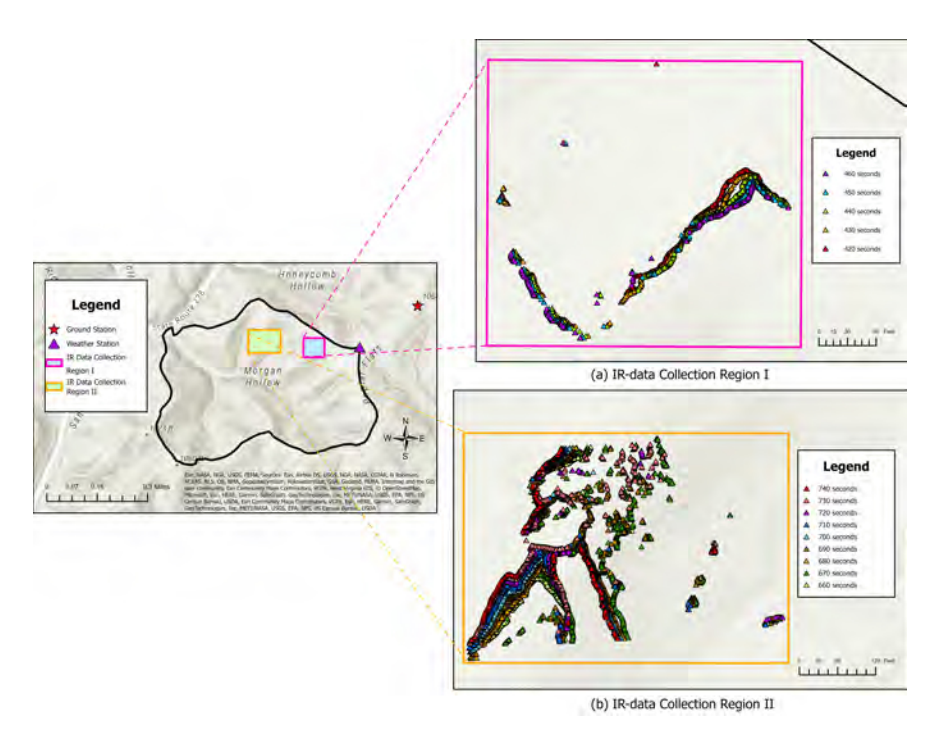


Fig. 13 IR-data Collection Areas

and $80.96\ ft/min$. This local study area has a global mean of $15.57\ ft/min$. From an operational standpoint, the global mean ROS holds little value for decision-making about fire management. On the other hand, the minimum and maximum ROS (along with the geographical locations of these rates) are important parameters that fire management professionals need accurate estimates of.

Table 4 Statistical Analysis of Region I

Time Stamp (s)	Number of points	Minimum (ft/min)	Maximum (ft/min)	Mean (ft/min)
420	247	2.49	54.97	16.92
430	355	2.71	60.79	17.60
440	331	2.19	55.72	16.10
450	259	0.93	80.96	15.06
460	192	0.99	27.28	9.84
	Total Num- ber of points	Global Min. (ft/min)	Global Max. (ft/min)	Global Mean (ft/min)
	1384	0.93	80.96	15.57

IR-data Collection in Region II

As presented in Table 5, a total of 5428 points were evaluated during nine 10-second intervals for Region II. The IR-based ROS statistical analysis demonstrates that the ROS range lies between 0.38 ft/min and 121.47 ft/min. The global mean is 18.23 ft/min for this local study area.

Table 5 Statistical Analysis of Region II

Time Stamp (s)	Number of points		Maximum (ft/min)	Mean (ft/min)
660	710	1.97	121.47	18.58
670	804	1.44	65.13	20.78
680	712	2.23	77.12	22.96
690	846	1.61	67.64	16.99
700	407	0.96	63.95	20.88
710	554	4.03	56.66	20.47
720	350	0.38	50.77	16.73
730	651	1.53	42.78	12.22
740	394	3.99	31.51	11.97
	Total Num- ber of points	Global Min. (ft/min)	Global Max. (ft/min)	Global Mean (ft/min)
	5428	0.38	121.47	18.23

B. Rothermel Model ROS Estimates

1. Data Collection and Processing

Starting the first week of June 2022, field trips were conducted to the study area at least three times per week, as described in Sec. (III.A). Field trips continued until August 2022 to collect relevant research data, including canopy closure, fuel depth, slope aspect, and slope steepness. As shown in Fig. (1(b)), 94 test locations were designated within Morgan Hollow for this study. These 94 locations were selected based on human accessibility by foot, and each point

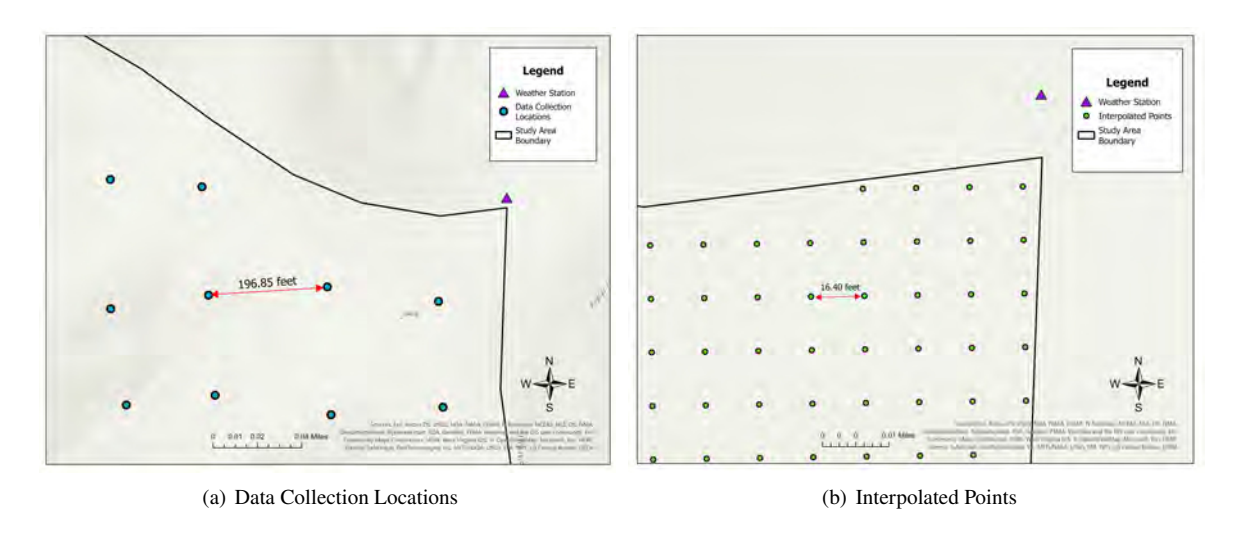


Fig. 14 Data Collection Locations against Interpolated Points

was set approximately 60 m (196.9 ft) away from each other, as illustrated in Fig.(14(a)).

One of the main components of environmental input parameters in the Rothermel model is slope steepness. The Sunnto PM-5/360 PC Clinometer was used to measure the steepness at each of the 94 study locations. The other two environmental components are wind speed and fuel moisture content. To capture the most accurate weather data, the weather station was installed at the highest possible location while being near the prescribed burn ignition points. As

shown in Fig.(1(b)), the selected point is located in the northern-east region of the study area $(82^{\circ}3015^{\circ}W, 39^{\circ}3619^{\circ}N)$ and elevated at 1059.71 ft above sea level. The Davis Vantage Vue Wireless Integrated Sensor Suite Weather Station and the Davis Vantage Vue® Wireless Console/Receiver were used to collect weather data: wind speed, dry bulb temperature, and relative humidity.

Note that ninety-four points provide only a relatively low-resolution estimate of ROS in a study area as large as Morgan Hollow, which covers approximately 58 hectares. ArcGIS Pro raster tools were utilized at interpolation points. Fig. (15) shows the sequence of steps followed for this process.

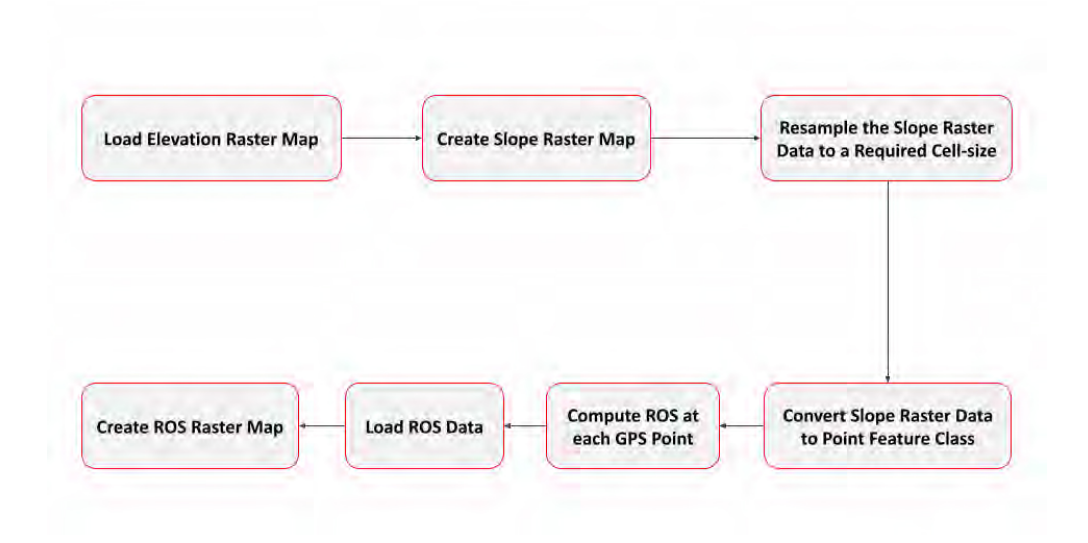


Fig. 15 Data Processing Flowchart

First, a slope raster map is generated in ArcGIS Pro by loading a digital elevation model (DEM) data [63] of the study area. The elevation raster map is then converted to a slope raster map using the slope (Spatial Analyst) toolbox. Then, the resolution of the original slope raster map is transformed to produce a new raster map with $5 m \times 5 m$ pixel dimensions by utilizing the resample (Data Management) toolbox. Next, the resampled slope raster data is converted to the point feature class to obtain slope steepness. In this step, the Raster to Point (Conversion) Toolbox is employed to create a layer of 22,922 points to represent the study area and ROS calculations. Finally, the resulting ROS data is loaded onto ArcGIS Pro, and the point to raster (Conversion) toolbox is employed to interpolate ROS data onto a raster map. Both the slope steepness raster map and the ROS raster map of the study area are displayed in Fig.(17).

2. Rothermel Model ROS Output

Table (6) contains the calculated Rothermel's ROS value based on the mean values of wind speed (ft/min), fuel moisture content (FMI percentage), and slope steepness (percentage). The mean values of each weather input parameter were calculated by finding the mean over 241 data-collecting instances during the 4-hr prescribed burn mission. The resultant "mean ROS" across the 94 study locations is 12.04 ft/min. We reiterate that this is the output of the Rothermel model using mean input parameter values for all environmental parameters (fuel moisture, topography, and wind). As mentioned before, this metric (average ROS across the spatial domain) has only mathematical significance and does not provide operational value.

Table 6 ROS Predicted by the Rothermel Model Using the Mean Values of Environmental Variables Across all 94 Data Collection Points

Mean Wind Speed (ft/min)	Mean FMI Value (%)	Mean Slope Steepness (%)	Mean-based Rate of Spread (ft/min)
235.51	11.65	58.98	12.04

The Rothermel model was employed as the next step to determine the ROS estimate at each of the 94 data collection locations across the study area. The Rothermel model has no explicit time dependency. The value of slope steepness varies across these locations. Wind speed and fuel moisture content measurements are only available from the singular weather station location. Fig.(16) shows the variability in ROS estimates across the data-collection sites against each of these four environmental parameters, separately. Fig.(16(a)) shows the variation in ROS estimate with respect to slope steepness across the study site. Mean values for each of the other input parameters (wind speed and FMI) are used in this plot. There are 94 ROS estimates shown (magenta circles), one corresponding to each data collection site. The mean ROS is also shown (blue diamond). The results of this plot are also summarized in Table (7). Together, they indicate that the slope steepness shows significant variation across the study area (minimum tan $\phi = 3.49$, maximum tan $\phi = 160.03$), and this causes a drastic variation in ROS across these points, ranging from a minimum ROS of 5.27 ft/min to 55.27 ft/min: a 949.13% variation between the slowest moving and fastest moving fire fronts.

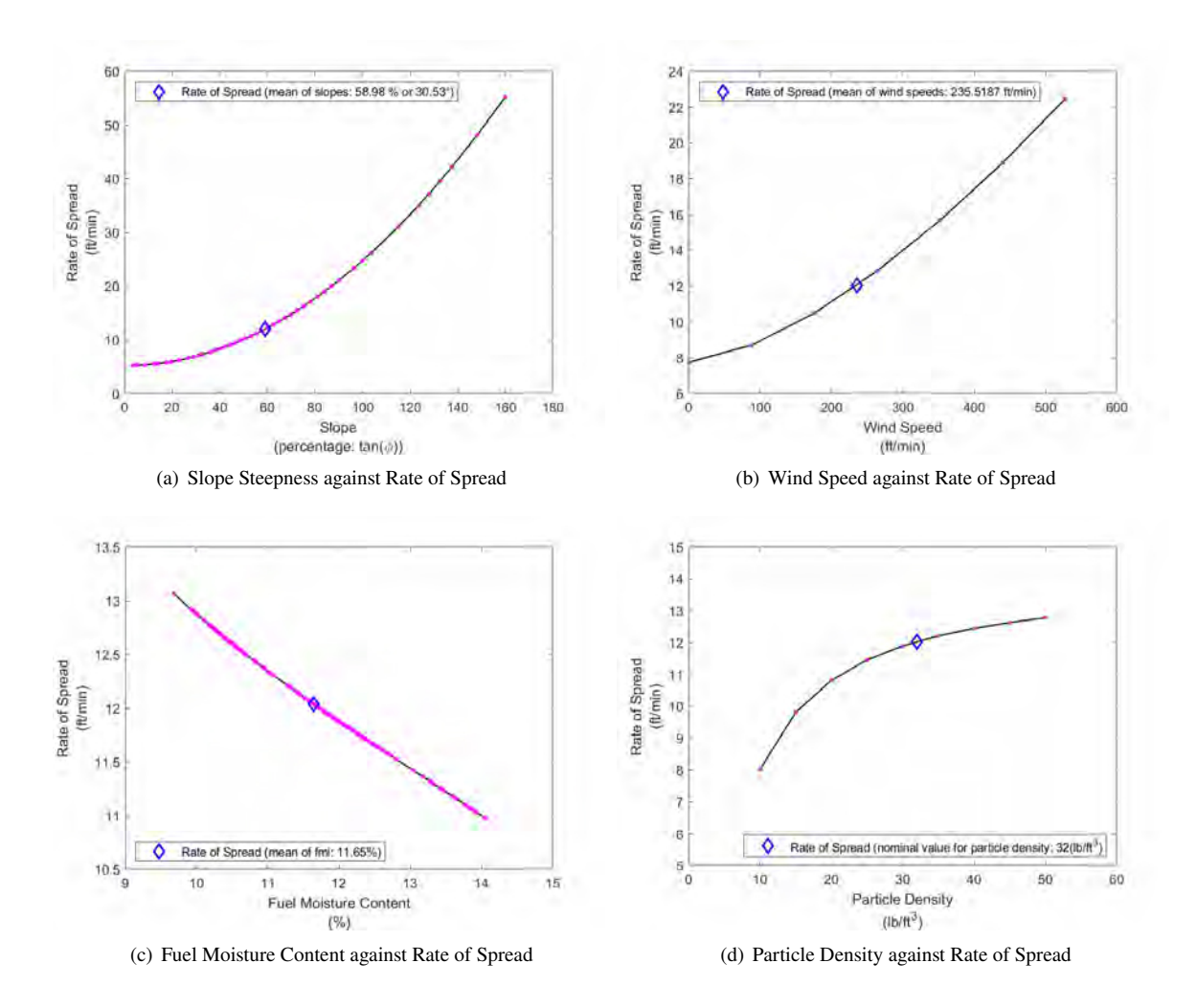


Fig. 16 Rothermel ROS Estimates at Data Collection Sites (94 Locations)

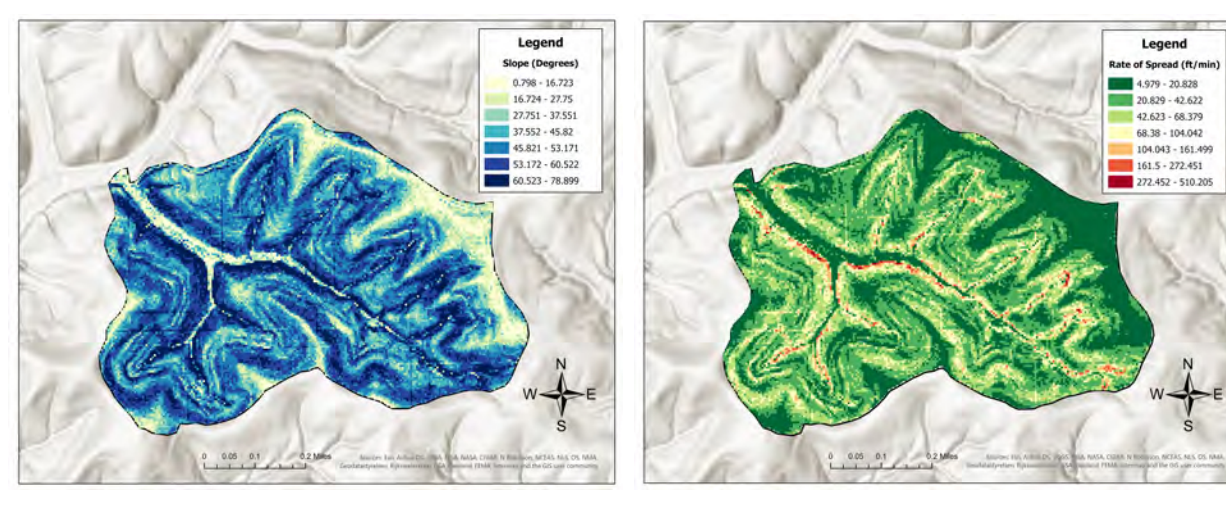
Fig.(16(b)) shows the variability of Rothermel's predicted ROS at the burn site with respect to measured wind speed. Wind can have a major impact on the fire rate of spread. The day of the prescribed burn at the study site was relatively calm, as seen from the measured wind speed values on the x-axis (measurements range between 0 mph and 6 mph). Using mean values for other parameters, the variation of ROS is shown on the y-axis and the second row of Table (7). Given the calm nature of the day of the burn, the Rothermel model predicts a relatively lower range of variation in predicted ROS. Fig.(16(c)) shows a similar study with respect to fuel moisture content, indicating that the variability across the burn site is low and, consequently, it does not impact ROS as much as slope steepness or wind speed. This is

Table 7 Rothermel ROS Output at Data-Collection Sites (94 Locations): Statistical Distribution of ROS Against Various Environmental Parameters

Input Variables	Mean ROS (ft/min)	Min. ROS (ft/min)	Max. ROS (ft/min)	Percentage Variability (%)
Slope Steepness	15.37	5.27	55.27	949.13
Wind Speed	12.50	7.76	22.48	189.51
FMI Percentage	12.06	10.98	13.07	19.02

confirmed in the third row of Table (7). Finally, Fig.(16(d)) shows the variation of ROS versus particle density. Note that particle density was assumed constant throughout the burn site. In order to illustrate the dependency of the ROS estimate on this variable, we show the impact of an arbitrary variation (9 equally spaced data points selected in the 10 - $50 lb/ft^3$ range), while holding mean values for slope steepness, wind speed, and the FMI. The resulting plot is similar to the results shown in Fig.13(b) of Ref.[25]. The results shown in Fig.(16) and Table (7) confirm that slope steepness and wind speed are the top two parameters that impact ROS estimates.

None of the results presented so far illustrate an adequate geographical (spatial) distribution of ROS. Note that a spatial distribution across the 94 data points will produce a coarse (low-resolution) map because of the low density of these points relative to the large size of the burn site. This is a major, real-life challenge during prescribed burns, especially in difficult, large terrains. In this study, we employ ArcGIS Pro to interpolate environmental parameters over the entire burn site using the measured values at the data collection points. As described in Sec.(IV.B.1), 22,922 points were generated and subsequently employed to produce a smooth ROS estimate across the entire burn site. Results are shown in Fig.(17). The result of slope steepness interpolation across the burn site is shown in Fig.(17(a)). The corresponding ROS outputs are shown in Fig.(17(b)).



(a) (Interpolated) Slope Steepness

(b) (Interpolated) Rate of Spread

Fig. 17 Intensity Comparison: Slope Steepness against Rate of Spread Interpolated Across the Burn Site

Table 8 displays the computed mean ROS output across all interpolation points, using the mean of each environmental parameter as the input to the Rothermel model. Between this table and Table (6), the only difference is in the mean value of slope steepness, which is significant, and indicates the dangers of having coarse field data. Clearly, interpolation induces a major difference in the mean value of the slope, leading to a major difference in the predicted ROS.

Finally, analogous to the results shown in Table (7), it is clearly seen in Table (9) that Rothermel ROS prediction has a high sensitivity to slope steepness. Slope steepness varies between a minimum of $\tan \phi = 1.39$ to a maximum of $\tan \phi = 509.67$. Over this range, a 9668.04% variation in the ROS output is observed.

Table 8 ROS Predicted by the Rothermel Model Using the Mean Values of Environmental Variables Across all 22,922 Interpolation Points in the Burn Site

Mean Wind Speed (ft/min)	Mean FMI Value (%)	Mean Slope Steepness (%)	Mean-based Rate of Spread (ft/min)
235.51	11.65	104.02	26.38

Table 9 Rothermel ROS Output at Interpolation Points (22,922 Locations): Statistical Distribution of ROS Against Various Environmental Parameters

Input Variables	Mean ROS (ft/min)	Min. ROS (ft/min)	Max. ROS (ft/min)	Percentage Difference (%)
Slope Steepness	37.93	5.25	512.60	9668.04
Wind Speed	26.84	22.10	36.82	66.56
FMI Percentage	26.43	24.06	28.64	19.05

C. Output Evaluation: IR-Data vs. Rothermel Model

Rothermel's model must be evaluated at the points where the fire is spreading in the infrared images to compare the output of Rothermel's Model with the ROS computed using the infrared images. This is done by interpolating the georeferenced points of the raster map to find the slope and Rothermel ROS at each point within the observed areas. As can be seen in Fig.(18), Rothermel's expected ROS and the infrared image ROS at each point are plotted against the interpolated slope angle at that point. The resulting trend is that Rothermel's Model underestimates the ROS when

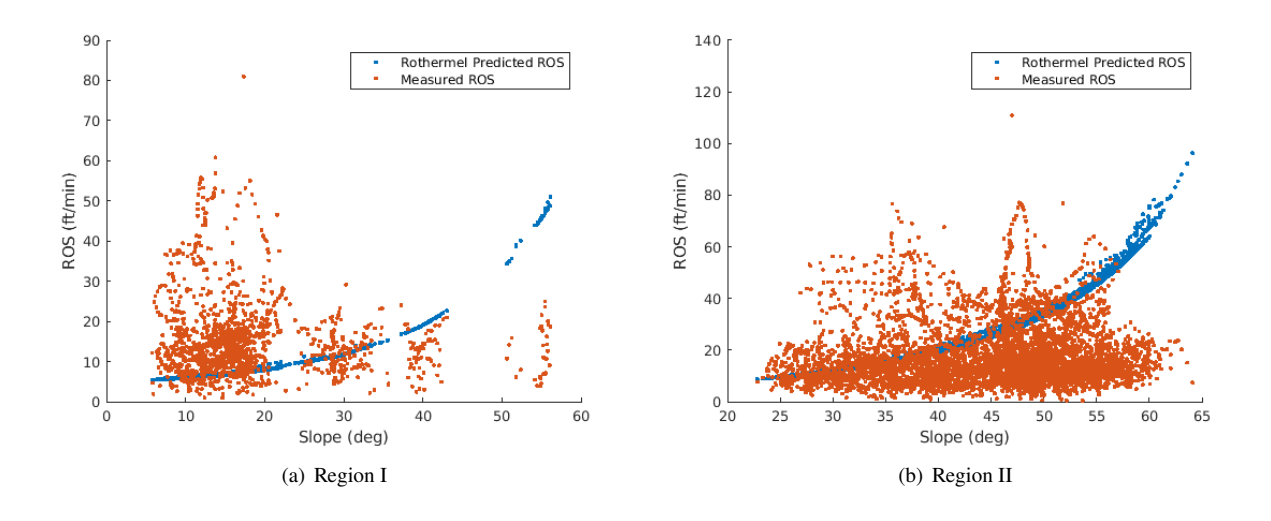


Fig. 18 ROS computed using IR-Data (Sec.(III)) compared with Rothermel's Model while varying slope.

the ground is flat, e.g., low slope. Additionally, it overestimates the ROS when the ground is steep, e.g. the slope is high. This can be attributed to several factors. First, Rothermel's model does not distinguish if the fire is traveling up or down the slope, so the underestimate may be due to the fact that the fire was traveling down the slope. Second, the underestimation when the slope is low can be attributed to factors such as wind velocity or moisture content that can result in a fast-moving fire front even on flat ground. Finally, errors propagated from re-projecting the infrared image into the terrain surface as described in Sec.(III.D) can result in both an incorrect slope estimate and an incorrect ROS estimate.

V. Conclusion

In this work a novel method to estimate the rate of spread of a wildfire is developed. Using infrared video captured by a UAS the ROS of a prescribed wildland burn can be computed without the need to pre-select the infrared contours used to describe the fire front using properties of the fire intensity distribution. Data collected from the prescribed wildland burn at Ohio's Zaleski State Forest in addition to data collected by the UAS is used in Rothermel's Model to compute the expected ROS within the study area. Comparing the output of Rothermel's model to the ROS computed using infrared images it is observed that Rothermel's model is able to accurately predict the observed ROS at a large scale, but when used at a local scale on a fire front it is unable to provide accurate estimates. Future work includes integrating path planning and situational awareness capabilities into the UAS to allow for increased autonomy in tracking the spreading of fire. Additionally, the re-projection method will be improved to avoid errors propagating that affect the estimated ROS.

Acknowledgments

The authors acknowledge support for this work from the National Science Foundation award number 2132798 under the NRI 3.0: Innovations in Integration of Robotics Program.

References

- [1] Bowman, D. M. J. S., Balch, J. K., Artaxo, P., Bond, W. J., Carlson, J. M., Cochrane, M. A., D'Antonio, C. M., DeFries, R. S., Doyle, J. C., Harrison, S. P., Johnston, F. H., Keeley, J. E., Krawchuk, M. A., Kull, C. A., Marston, J. B., Moritz, M. A., Prentice, I. C., Roos, C. I., Scott, A. C., Swetnam, T. W., van der Werf, G. R., and Pyne, S. J., "Fire in the Earth System," *Science*, Vol. 324, No. 5926, 2009, pp. 481–484. https://doi.org/10.1126/science.1163886, URL https://www.science.org/doi/abs/10.1126/science.1163886.
- [2] Allen, C. D., Savage, M., Falk, D. A., Suckling, K. F., Swetnam, T. W., Schulke, T., Stacey, P. B., Morgan, P., Hoffman, M., and Klingel, J. T., "Ecological Restoration Of Southwestern Ponderosa Pine Ecosystems: A Broad Perspective," *Ecological Applications*, Vol. 12, No. 5, 2002, pp. 1418–1433. https://doi.org/https://doi.org/10.1890/1051-0761(2002)012[1418: EROSPP]2.0.CO;2.
- [3] Abatzoglou, J. T., and Williams, A. P., "Impact of anthropogenic climate change on wildfire across western US forests," *Proceedings of the National Academy of Sciences*, Vol. 113, No. 42, 2016, pp. 11770–11775. https://doi.org/10.1073/pnas. 1607171113, URL https://www.pnas.org/doi/abs/10.1073/pnas.1607171113.
- [4] Westerling, A. L., "Increasing western US forest wildfire activity: sensitivity to changes in the timing of spring," *Philosophical Transactions of the Royal Society B: Biological Sciences*, Vol. 371, No. 1696, 2016, p. 20150178. https://doi.org/10.1098/rstb. 2015.0178, URL https://royalsocietypublishing.org/doi/abs/10.1098/rstb.2015.0178.
- [5] Feurdean, A., Florescu, G., Tanţău, I., Vannière, B., Diaconu, A.-C., Pfeiffer, M., Warren, D., Hutchinson, S. M., Gorina, N., Gałka, M., and Kirpotin, S., "Recent fire regime in the southern boreal forests of western Siberia is unprecedented in the last five millennia," *Quaternary Science Reviews*, Vol. 244, 2020, p. 106495. https://doi.org/10.1016/j.quascirev. 2020.106495, URL https://www.sciencedirect.com/science/article/pii/S0277379120304571.
- [6] Westerling, A. L., Turner, M. G., Smithwick, E. A. H., Romme, W. H., and Ryan, M. G., "Continued warming could transform Greater Yellowstone fire regimes by mid-21st century," *Proceedings of the National Academy of Sciences*, Vol. 108, No. 32, 2011, pp. 13165–13170. https://doi.org/10.1073/pnas.1110199108, URL https://www.pnas.org/doi/abs/10.1073/pnas.1110199108.
- [7] Dennison, P. E., Brewer, S. C., Arnold, J. D., and Moritz, M. A., "Large wildfire trends in the western United States, 1984–2011," *Geophysical Research Letters*, Vol. 41, No. 8, 2014, pp. 2928–2933. https://doi.org/https://doi.org/10.1002/2014GL059576, URL https://agupubs.onlinelibrary.wiley.com/doi/abs/10.1002/2014GL059576.
- [8] Flannigan, M., Krawchuk, M., Wotton, M., and Johnston, L., "Implications of changing climate for global Wildland fire," International Journal of Wildland Fire, Vol. 18, 2009, pp. 483–507. https://doi.org/10.1071/WF08187.
- [9] Falk, D. A., Heyerdahl, E. K., Brown, P. M., Farris, C., Fulé, P. Z., McKenzie, D., Swetnam, T. W., Taylor, A. H., and Van Horne, M. L., "Multi-scale controls of historical forest-fire regimes: new insights from fire-scar networks," *Frontiers in Ecology and the Environment*, Vol. 9, No. 8, 2011, pp. 446–454. https://doi.org/https://doi.org/10.1890/100052, URL https://esajournals.onlinelibrary.wiley.com/doi/abs/10.1890/100052.

- [10] Hilton, J., Miller, C., Sullivan, A., and Rucinski, C., "Effects of spatial and temporal variation in environmental conditions on simulation of wildfire spread," *Environmental Modelling and Software*, Vol. 67, 2015, pp. 118–127. https://doi.org/https://doi.org/10.1016/j.envsoft.2015.01.015, URL https://www.sciencedirect.com/science/article/pii/S1364815215000468.
- [11] Morandini, F., Silvani, X., Rossi, L., Santoni, P.-A., Simeoni, A., Balbi, J.-H., Louis Rossi, J., and Marcelli, T., "Fire spread experiment across Mediterranean shrub: Influence of wind on flame front properties," *Fire Safety Journal*, Vol. 41, No. 3, 2006, pp. 229–235. https://doi.org/10.1016/j.firesaf.2006.01.006, URL https://www.sciencedirect.com/science/article/pii/S0379711206000191.
- [12] Gowravaram, S., Chao, H., Lin, Z., Parsons, S., Zhao, T., Xin, M., Hu, X., Tian, P., Flanagan, H. P., and Wang, G., "Prescribed Grass Fire Mapping and Rate of Spread Measurement Using NIR Images From a Small Fixed-Wing UAS," *IEEE Journal of Selected Topics in Applied Earth Observations and Remote Sensing*, Vol. 16, 2023, pp. 3519–3530. https://doi.org/10.1109/JSTARS.2023.3255230.
- [13] Holsinger, L., Parks, S. A., and Miller, C., "Weather, fuels, and topography impede wildland fire spread in western US landscapes," *Forest Ecology and Management*, Vol. 380, 2016, pp. 59–69. https://doi.org/https://doi.org/10.1016/j.foreco.2016.08.035, URL https://www.sciencedirect.com/science/article/pii/S0378112716304583, special section: Drought and US Forests: Impacts and Potential Management Responses.
- [14] Stow, D., Riggan, P., Schag, G., Brewer, W., Tissell, R., Coen, J., and Storey, E., "Assessing uncertainty and demonstrating the potential for estimating fire rate of spread at landscape scales based on time-sequential airborne thermal infrared imaging," *International Journal of Remote Sensing*, Vol. 40, No. 13, 2019, pp. 4876–4897. https://doi.org/10.1080/01431161.2019.1574995, URL https://doi.org/10.1080/01431161.2019.1574995.
- [15] Abrams, M. D., "Fire and the Development of Oak Forests: In eastern North America, oak distribution reflects a variety of ecological paths and disturbance conditions," *BioScience*, Vol. 42, No. 5, 1992, pp. 346–353. https://doi.org/10.2307/1311781, URL https://doi.org/10.2307/1311781.
- [16] Agee, J., Fire Ecology of Pacific Northwest Forests, Island Press, 1993. URL https://books.google.com/books?id=kADxAAAMAAJ.
- [17] Pausas, J. G., and Keeley, J. E., "A Burning Story: The Role of Fire in the History of Life," *BioScience*, Vol. 59, No. 7, 2009, pp. 593–601. https://doi.org/10.1525/bio.2009.59.7.10, URL https://doi.org/10.1525/bio.2009.59.7.10.
- [18] Ryan, K. C., Knapp, E. E., and Varner, J. M., "Prescribed fire in North American forests and woodlands: history, current practice, and challenges," *Frontiers in Ecology and the Environment*, Vol. 11, No. s1, 2013. https://doi.org/10.1890/120329, URL https://doi.org/10.1890/120329.
- [19] Covington, W. W., and Moore, M. M., "Postsettlement Changes in Natural Fire Regimes and Forest Structure," *Journal of Sustainable Forestry*, Vol. 2, 1994, pp. 153–181. https://doi.org/10.1300/J091v02n01_07, URL https://doi.org/10.1300/J091v02n01_07.
- [20] Keane, R. E., Ryan, K. C., Veblen, T. T., Allen, C. D., Logan, J., and Hawkes, B., "Cascading effects of fire exclusion in the Rocky Mountain ecosystems: a literature review," Tech. rep., 2002. https://doi.org/10.2737/rmrs-gtr-91, URL https://doi.org/10.2737/RMRS-GTR-91.
- [21] Varner, J. M., Gordon, D. R., Putz, F. E., and Hiers, J. K., "Restoring Fire to Long-Unburned Pinus palustris Ecosystems: Novel Fire Effects and Consequences for Long-Unburned Ecosystems," *Restoration Ecology*, Vol. 13, No. 3, 2005, pp. 536–544. https://doi.org/10.1111/j.1526-100x.2005.00067.x, URL https://doi.org/10.1111/j.1526-100x.2005.00067.x.
- [22] Noss, R. F., Beier, P., Wallace Covington, W., Edward Grumbine, R., Lindenmayer, D. B., Prather, J. W., Schmiegelow, F., Sisk, T. D., and Vosick, D. J., "Recommendations for Integrating Restoration Ecology and Conservation Biology in Ponderosa Pine Forests of the Southwestern United States," *Restoration Ecology*, Vol. 14, No. 1, 2006, pp. 4–10. https://doi.org/https://doi.org/10.1111/j.1526-100X.2006.00099.x, URL https://onlinelibrary.wiley.com/doi/abs/10.1111/j.1526-100X.2006.00099.x.
- [23] Kerns, B. K., and Day, M. A., "Prescribed fire regimes subtly alter ponderosa pine forest plant community structure," *Ecosphere*, Vol. 9, No. 12, 2018, p. e02529. https://doi.org/https://doi.org/10.1002/ecs2.2529, URL https://esajournals.onlinelibrary.wiley.com/doi/abs/10.1002/ecs2.2529.
- [24] Mahood, A. L., and Balch, J. K., "Repeated fires reduce plant diversity in low-elevation Wyoming big sagebrush ecosystems (1984–2014)," *Ecosphere*, Vol. 10, No. 2, 2019, p. e02591. https://doi.org/https://doi.org/10.1002/ecs2.2591, URL https://esajournals.onlinelibrary.wiley.com/doi/abs/10.1002/ecs2.2591.

- [25] Andrews, P. L., "The Rothermel surface fire spread model and associated developments: A comprehensive explanation," Tech. rep., 2018. https://doi.org/10.2737/rmrs-gtr-371, URL https://www.fs.usda.gov/research/treesearch/55928.
- [26] Alexander, M. E., and Cruz, M. G., Fireline Intensity, Springer International Publishing, 2018, pp. 1–8. https://doi.org/10.1007/978-3-319-51727-8_52-1, URL https://doi.org/10.1007/978-3-319-51727-8_52-1.
- [27] Williams, R. J., Gill, A. M., and Moore, P. H., Fire Behavior, Springer New York, New York, NY, 2003, pp. 33–46. https://doi.org/10.1007/0-387-21515-8_3, URL https://doi.org/10.1007/0-387-21515-8_3.
- [28] Werth, P. A., Potter, B. E., Clements, C. B., Finney, M. A., Goodrick, S. L., Alexander, M. E., Cruz, M. G., Forthofer, J. A., and McAllister, S. S., "Synthesis of knowledge of extreme fire behavior: volume I for fire managers," Tech. rep., 2011. https://doi.org/10.2737/pnw-gtr-854, URL https://doi.org/10.2737/PNW-GTR-854.
- [29] Castellnou, M., Kraus, D., Miralles, M., and Delogu, G., "5.2 Suppression Fire Use in Learning Organizations," *Towards Integrated Fire Management Outcomes of the European Project Fire Paradox*, 2010, p. 189. URL https://efi.int/publications-bank/towards-integrated-fire-management-outcomes-european-project-fire-paradox.
- [30] Change, N. C., "Spreading like wildfire," Nature Climate Change, Vol. 7, No. 11, 2017, p. 755. URL https://doi.org/10.1038/nclimate3432.
- [31] Rodrigues, M., Angel Cunill Camprubí, Balaguer-Romano, R., Coco Megía, C. J., Castañares, F., Ruffault, J., Fernandes, P. M., and Resco de Dios, V., "Drivers and implications of the extreme 2022 wildfire season in Southwest Europe," *Science of The Total Environment*, Vol. 859, 2023, p. 160320. https://doi.org/https://doi.org/10.1016/j.scitotenv.2022.160320, URL https://www.sciencedirect.com/science/article/pii/S0048969722074204.
- [32] Chuvieco, E., Aguado, I., Salas, J., García, M., Yebra, M., and Oliva, P., "Satellite Remote Sensing Contributions to Wildland Fire Science and Management," *Current Forestry Reports*, Vol. 6, 2020, p. 81–96. https://doi.org/10.1007/s40725-020-00116-5.
- [33] Schroeder, W., Prins, E., Giglio, L., Csiszar, I., Schmidt, C., Morisette, J., and Morton, D., "Validation of GOES and MODIS active fire detection products using ASTER and ETM+ data," *Remote Sensing of Environment*, Vol. 112, 2008, p. 2711–2726. https://doi.org/10.1016/j.rse.2008.01.005.
- [34] Filizzola, C., Corrado, R., Marchese, F., Mazzeo, G., Paciello, R., Pergola, N., and Tramutoli, V., "RST-FIRES, an exportable algorithm for early-fire detection and monitoring: description, implementation, and field validation in the case of the MSG-SEVIRI sensor," *Remote Sensing of Environment*, Vol. 186, 2016, pp. 196–216. https://doi.org/10.1016/j.rse.2016.08.008.
- [35] Arroyo, L. A., Pascual, C., and Manzanera, J. A., "Fire models and methods to map fuel types: The role of remote sensing," *Forest Ecology and Management*, Vol. 256, 2008, p. 1239–1252. https://doi.org/10.1016/j.foreco.2008.06.048.
- [36] Bertolette, D. R., and Spotskey, D. B., "Fuel model and forest type mapping for FARSITE," *The Joint Fire Science Conference and Workshop*, University of Idaho and International Association of Wildland Fire, Boise, Idaho, 1999.
- [37] Dandois, J. P., Olano, M., and Ellis, E. C., "Optimal Altitude, Overlap, and Weather Conditions for Computer Vision UAV Estimates of Forest Structure," *Remote Sensing*, Vol. 7, No. 10, 2015, p. 13895–13920. https://doi.org/10.3390/rs71013895.
- [38] Reilly, S., Clark, M. L., Bentley, L. P., Matley, C., Piazza, E., and Menor, I. O., "The Potential of Multispectral Imagery and 3D Point Clouds from Unoccupied Aerial Systems (UAS) for Monitoring Forest Structure and the Impacts of Wildfire in Mediterranean-Climate Forests," *Remote Sensing*, Vol. 13, 2021, p. 3810. https://doi.org/10.3390/rs13193810.
- [39] Schag, G. M., Stow, D. A., Riggan, P. J., and Nara, A., "Spatial-Statistical Analysis of Landscape-Level Wildfire Rate of Spread," *Remote Sensing*, Vol. 14, No. 16, 2022. https://doi.org/10.3390/rs14163980, URL https://www.mdpi.com/2072-4292/14/16/3980.
- [40] Ottmar, R., Watts, A., Larkin, S., Brown, T., and French, N., "Final Report: Fire and Smoke Model Evaluation Experiment (FASMEE) Phase 2," Tech. Rep. JFSP Project ID: 15-S-01-01, Joint Fire Science Program (JSFP), Dec, 2021.
- [41] Johnston, J. M., Wheatley, M. J., Wooster, M. J., Paugam, R., Davies, G. M., and DeBoer, K. A., "Flame-Front Rate of Spread Estimates for Moderate Scale Experimental Fires Are Strongly Influenced by Measurement Approach," *Fire*, Vol. 1, No. 1, 2018. https://doi.org/10.3390/fire1010016, URL https://www.mdpi.com/2571-6255/1/1/16.
- [42] Alexander, M. E., "Fire behaviour as a factor in forest and rural fire suppression." 2000. URL https://www.semanticscholar.org/paper/Fire-behaviour-as-a-factor-in-forest-and-rural-fire-Alexander/f8e463ade8b80779c7920eaa3ae2e1cedb82cdaf.

- [43] Lopes, A., Cruz, M., and Viegas, D., "FireStation an integrated software system for the numerical simulation of fire spread on complex topography," *Environmental Modelling & Software*, Vol. 17, No. 3, 2002, pp. 269–285. https://doi.org/https://doi.org/10.1016/S1364-8152(01)00072-X, URL https://www.sciencedirect.com/science/article/pii/S136481520100072X.
- [44] Mangiameli, M., Mussumeci, G., and Cappello, A., "Forest Fire Spreading Using Free and Open-Source GIS Technologies," Geomatics, Vol. 1, No. 1, 2021, pp. 50–64. https://doi.org/10.3390/geomatics1010005, URL https://www.mdpi.com/2673-7418/1/1/5.
- [45] Martínez-de Dios, J. R., Merino, L., Caballero, F., and Ollero, A., "Automatic Forest-Fire Measuring Using Ground Stations and Unmanned Aerial Systems," Sensors, Vol. 11, No. 6, 2011, pp. 6328–6353. https://doi.org/10.3390/s110606328, URL https://www.mdpi.com/1424-8220/11/6/6328.
- [46] Sandberg, D. V., Riccardi, C. L., and Schaaf, M. D., "Reformulation of Rothermel's wildland fire behaviour model for heterogeneous fuelbedsThis article is one of a selection of papers published in the Special Forum on the Fuel Characteristic Classification System." *Canadian Journal of Forest Research*, Vol. 37, No. 12, 2007, pp. 2438–2455. https://doi.org/10.1139/X07-094, URL https://doi.org/10.1139/X07-094.
- [47] "QGroundControl Ground Control Station for MAVLink Protocol," http://qgroundcontrol.com/, 2023.
- [48] "MAVLink MAV Communication Protocol," https://mavlink.io/, 2023.
- [49] Zhai, C., Zhang, S., Cao, Z., and Wang, X., "Learning-based prediction of wildfire spread with real-time rate of spread measurement," *Combustion and Flame*, Vol. 215, 2020, pp. 333–341. https://doi.org/https://doi.org/10.1016/j.combustflame. 2020.02.007, URL https://www.sciencedirect.com/science/article/pii/S001021802030064X.
- [50] Planas, E., Cubells, M., and Pastor, E., "Different Approaches for the Head Fire Perimeter Definition in Wildland Fires," 2011, pp. 1425–1436. https://doi.org/10.3801/IAFSS.FSS.10-1425, URL https://publications.iafss.org/publications/fss/10/1425.
- [51] Pastor, E., Àgueda, A., Andrade-Cetto, J., Muñoz, M., Pérez, Y., and Planas, E., "Computing the rate of spread of linear flame fronts by thermal image processing," *Fire Safety Journal*, Vol. 41, No. 8, 2006, pp. 569–579. https://doi.org/10.1016/j.firesaf.2006.05.009, URL https://www.sciencedirect.com/science/article/pii/S0379711206000701.
- [52] Rothermel, R., A Mathematical Model for Predicting Fire Spread in Wildland Fuels, USDA Forest Service research paper INT, Intermountain Forest & Range Experiment Station, Forest Service, U.S. Department of Agriculture, 1972. URL https://books.google.com/books?id=AfyMv5NBSjoC.
- [53] Albini, F., Forest, I., and Range Experiment Station (Ogden, U., Computer-based Models of Wildland Fire Behavior: A User's Manual, Intermountain Forest and Range Experiment Station, Forest Service, U.S. Department of Agriculture, 1976. URL https://books.google.com/books?id=iJ9lMi9OvJYC.
- [54] Frandsen, W. H., "Fire spread through porous fuels from the conservation of energy," Combustion and Flame, Vol. 16, No. 1, 1971, pp. 9–16. https://doi.org/https://doi.org/10.1016/S0010-2180(71)80005-6, URL https://www.sciencedirect.com/science/article/pii/S0010218071800056.
- [55] Scott, J. H., and Burgan, R. E., "Standard fire behavior fuel models: a comprehensive set for use with Rothermel's surface fire spread model," Tech. rep., 2005. https://doi.org/10.2737/rmrs-gtr-153, URL https://doi.org/10.2737/RMRS-GTR-153.
- [56] Albini, F., Forest, I., Range Experiment Station (Ogden, U., and Service, U. S. F., *Estimating Wildfire Behavior and Effects*, General technical report INT, Department of Agriculture, Forest Service, Intermountain Forest, and Range Experiment Station, 1976. URL https://books.google.com/books?id=EfUTAAAAYAAJ.
- [57] Sullivan, A. L., "Wildland surface fire spread modelling, 1990 2007. 1: Physical and quasi-physical models," *International Journal of Wildland Fire*, Vol. 18, No. 4, 2009, p. 349. https://doi.org/10.1071/wf06143, URL https://www.publish.csiro.au/wf/WF06143.
- [58] Andrews, P. L., "Modeling wind adjustment factor and midflame wind speed for Rothermel's surface fire spread model," Tech. rep., 2012. https://doi.org/10.2737/rmrs-gtr-266, URL https://doi.org/10.2737/RMRS-GTR-266.
- [59] Simard, A. J., "The moisture content of forest fuels I: a review of the basic concepts," Tech. rep., 1968. URL https://cfs.nrcan.gc.ca/publications?id=24782.
- [60] Nelson Jr., R. M., "A method for describing equilibrium moisture content of forest fuels," Canadian Journal of Forest Research, Vol. 14, No. 4, 1984, pp. 597–600. https://doi.org/10.1139/x84-108, URL https://doi.org/10.1139/x84-108.

- [61] Pook, E., and Gill, A., "Variation of Live and Dead Fine Fuel Moisture in <I>Pinus radiata</I> Plantations of the Australian-Capital-Territory," *International Journal of Wildland Fire*, Vol. 3, No. 3, 1993, pp. 155–168. https://doi.org/https://doi.org/10. 1071/WF9930155.
- [62] Sharples, J., McRae, R., Weber, R., and Gill, A., "A simple index for assessing fuel moisture content," *Environmental Modelling & Software*, Vol. 24, No. 5, 2009, pp. 637–646. https://doi.org/https://doi.org/10.1016/j.envsoft.2008.10.012, URL https://www.sciencedirect.com/science/article/pii/S1364815208001886.
- [63] "The Ohio Geographically Referenced Information Program Geodata Download," https://gis1.oit.ohio.gov/geodatadownload/, 2023